

# Generalized Terahertz Perfect Vortices with Transmutable Intensity Profiles Based on Spin-Decoupled Geometric Metasurfaces

Bowen Sun, Xiaofei Zang,\* Binbin Lu, Haoxiang Chi, Yiwen Zhou, Yiming Zhu,\* and Songlin Zhuang

Perfect vortex beams (PVBs) possessing orbital angular momentum (OAM) and constant intensity profile enable practical applications in information encoding and transmission due to an unbounded number of orthogonal OAM channels and fixed annular intensity distributions. Geometric metasurfaces, which are 2D counterparts of metamaterials, have provided an ultra-compact platform to flexibly design perfect vortex beams in a single flat device. However, the previous reported PVBs based on geometric metasurfaces are limited to ring-shaped intensity profiles and intrinsic spin-coupling between two orthogonal spin-components. Here, spin-decoupled geometric metasurfaces encoding with two-step coordinate transformations are proposed to generate helicity-independent PVBs with transmutable intensity profiles. By tailoring local phase gradient along the azimuthal direction, spin-independent and polarization-rotated terahertz (THz) PVBs with  $C_N$ -fold rotationally symmetric intensity profiles have been theoretically designed and experimentally demonstrated. Furthermore, THz PVBs with arbitrary intensity profiles have also been realized. The unique approach for simultaneously manipulating the spiral phase, focusing phase, as well as intensity profiles will open a new avenue to develop multifunctional integrated devices and systems, which enables potential applications in information processing and optical communication.


applications of optical fiber communications, one needs to match the radial size of vortex beams to that of the fiber, which significantly limits the information capacity. Recently, the concept of perfect vortex beams (PVBs), which possess annular intensity profiles independent of topological charges, has been proposed to overcome the abovementioned limitations.<sup>[6]</sup> There are a variety of approaches to generating PVBs including spatial light modulators,<sup>[7,8]</sup>  $q$ -plates,<sup>[9]</sup> axicon lens,<sup>[10]</sup> and Fourier transform lens.<sup>[11]</sup> However, all these schemes (to generate PVBs) are traditionally relied on a series of bulky optical components, which cannot be simply downsized, preventing the development of miniaturized and integrated systems. In addition, the misalignment or incompatibility between these bulky optical components will inevitably degrade the quality of generated PVBs.

Geometric metasurfaces, which consist of pre-designed anisotropic meta-atoms with identical shape but different in-plane orientations, have unprecedented capabilities in precisely manipulating the amplitude, phase and polarization of EM waves.<sup>[12,13]</sup> Unlike traditional bulk devices that are dependent on gradual phase accumulations along an optical path to realize the desired wave-manipulating functionality, metasurface-based components rely on abrupt phase changes at planar meta-atom interfaces. Therefore, wavefront-modulation functionalities can be easily obtained just by accurately controlling the orientation of each meta-atom in geometric metasurfaces. Meanwhile, geometric metasurfaces provide a flexible platform for designing ultra-compact and high-performance components, which enable potential applications in device miniaturization and system integration. Therefore, a plethora of studies ranging from fundamental science to practical applications, that is, the generalized Snell's law,<sup>[14–16]</sup> polarization control and analysis,<sup>[17–19]</sup> spin-Hall effects,<sup>[20–22]</sup> metalenses,<sup>[23–30]</sup> and holograms,<sup>[31–36]</sup> have been demonstrated. Geometric metasurfaces can be also designed to generate and manipulate vortex beams such as the generation of vortex beams,<sup>[37–40]</sup> vortex multiplexing,<sup>[41,42]</sup> and vector vortex beams.<sup>[43–45]</sup> Recently, metasurfaces also have been proposed to

## 1. Introduction

Electromagnetic (EM) waves possessing orbital angular momentum (OAM), which are named as vortex beams, have attracted considerable attention in fields ranging from quantum science to optical communications.<sup>[1–4]</sup> Because of phase singularity, a vortex beam always shows a dark central spot surrounded by a bright ring, and the radius (of the bright ring) is related to corresponding topological charges.<sup>[5]</sup> For one of the most important

B. Sun, X. Zang, B. Lu, H. Chi, Y. Zhou, Y. Zhu, S. Zhuang  
Terahertz Technology Innovation Research Institute, and Shanghai Key  
Lab of Modern Optical System  
University of Shanghai for Science and Technology  
No. 516 JunGong Road, Shanghai 200093, China  
E-mail: xfzang@usst.edu.cn; ymzhu@usst.edu.cn

 The ORCID identification number(s) for the author(s) of this article can be found under <https://doi.org/10.1002/adom.202301048>

DOI: 10.1002/adom.202301048

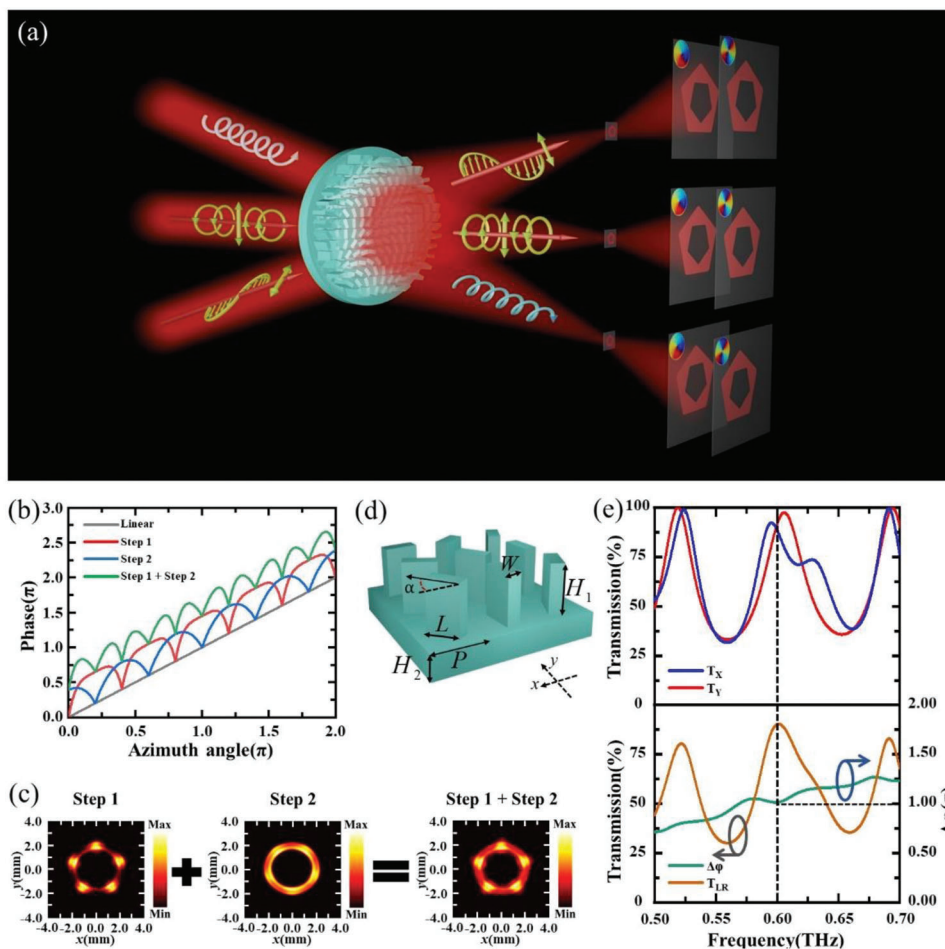


**Figure 1.** The schematic and operating principle of geometric metasurfaces for generating THz PVBs with transmutable intensity profiles. a) The schematic of a geometric metasurface for generating spin-dependent, spin-decoupled and polarization-rotated PVBs with transmutable intensity profiles. b) The phase requirements for a traditional ring-shaped PVB (gray curve) and a PVB with transmutable intensity profile (red-dot, blue-dot and green curves), and the topological charges of these PVBs are  $l_L = 1$ . c) The comparison of intensity distributions (of PVBs with topological charge of 1) of metasurfaces with only the first and two-steps of coordinate transformations. The working frequency is 0.6 THz. d) The schematic of a geometric metasurface. e) The transmission spectra (top) of the x-polarized (blue curve) and y-polarized (red curve) incidence of THz waves. The polarization conversion efficiency for the incidence of RCP waves is shown as the orange curve, while the phase difference between the transmitted x-polarized and y-polarized THz waves is shown as the green curve.

realize PVBs by integrating the functionalities of a spiral phase plate, an axicon lens and a Fourier transform lens into a single flat device.<sup>[46–49]</sup> The reported approaches for generating PVBs are relied on the simulated phase and amplitude modulation, and the complicated oblique incidence scheme or both dynamic and geometric phase modulations. In addition, the main reported PVBs are limited to the ring-shaped intensity profiles. How to generate PVBs with transmutable intensity profiles by pure geometric phase (which can avoid scanning a large number of parameters to achieve desired unit cells) has not attracted wide attention yet.

In this paper, the terahertz (THz) PVBs with transmutable intensity profiles realized by spin-decoupled geometric metasurfaces are proposed and experimentally demonstrated. The multiple functionalities in generating PVBs and manipulating their corresponding intensity profiles are simultaneously realized by integrating the spiral phase, axicon lens, Fourier transform lens and two types of azimuthal nonlinear phases into

a spin-decoupled geometric metasurface (consisting of meta-atoms with identical shape but different in-plane orientations). In experiment, the generation of THz spin-independent and polarization-rotated PVBs with  $C_5$ -fold rotationally symmetric intensity distributions have been demonstrated. Furthermore, the THz PVBs with arbitrary closed-loop profiles are also proposed and demonstrated. The robust and unique approach for generating PVBs with transmutable intensity profiles may open a new window for designing multifunctional devices and promote the development of integrated system.

## 2. Methodology

The generation of THz PVBs with transmutable intensity profiles is schematically shown in **Figure 1**. The geometric metasurface consists of a variety of anisotropic (silicon-based) meta-atoms with identical shape but different orientations. By delicately

controlling in-plane orientations of each meta-atom, the required phase profile can be encoded into such a metasurface to generate THz PVBs with transmutable intensity profiles. As shown by Figure 1 for the left-handed circularly polarized (LCP) incident THz beam, a right-handed circularly polarized (RCP) PVB with  $C_5$ -fold (pentagon) rotationally symmetric intensity profiles can be generated. By breaking intrinsic spin-locking and adding the polarization-rotated functionality into such a metasurface, the helicity-independent and polarization-rotated THz PVBs with transmutable intensity profiles can be also realized.

For the generation of a spin-dependent PVB (perfect vortex beam), the functionalities of spiral phase plate, Fourier transform lens, and axicon lens, should be encoded into a metasurface and the corresponding phase requirement is governed by

$$\varphi_{\text{LCP}} = \varphi_{\text{spiral}} + \varphi_{\text{lens}} + \varphi_{\text{axicon}} \quad (1)$$

where  $\varphi_{\text{spiral}} = l_L \phi$  (to generate a vortex beam),  $\varphi_{\text{lens}} = \frac{2\pi}{\lambda} (\sqrt{(x-x_1)^2 + (y-y_1)^2} + f - f)$  (to further generate a Bessel-Gaussian beam), and  $\varphi_{\text{axicon}} = \frac{2\pi}{d} \sqrt{(x-x_2)^2 + (y-y_2)^2}$  (to finally generate a PVB), and  $\lambda$  is the operating wavelength, while  $f$  is the focal length of the Fourier transform lens.  $\phi$  is the azimuthal angle, which is defined as  $\phi = \arctan(\frac{y}{x})$ .  $l_L$  is the topological charge of the generated PVB, and  $d$  ( $= 4.2$  mm) is the period of the axicon lens. In this work, the abovementioned parameters are selected as  $\lambda = 0.5$  mm (0.6 THz),  $f = 15$  mm.

For  $x_1 = x_2 = y_1 = y_2 = 0$ , the traditional (RCP) PVB with a ring-shaped intensity profile (or  $O(2)$  continuous rotational symmetry) can be generated under the illumination of a LCP beam. To breaking the  $O(2)$  rotational symmetry in the intensity profile, we introduce two-step coordinate transformations to generate PVBs with transmutable intensity profiles. As an example, the PVBs with  $C_N$ -fold rotationally symmetric intensity profiles are designed, and the first step (Figure 1b of red-dot curve) of coordinate transformations (added in the Fourier transform lens) can be expressed as follows

$$x_1 = (r_\phi - r_1) \cos(\varphi_1 + \phi) \quad (2)$$

$$y_1 = (r_\phi - r_1) \sin(\varphi_1 + \phi) \quad (3)$$

$$r_\phi = \frac{r_0}{\cos(\pi/N - \text{mod}(\phi, 2\pi/N))} \quad (4)$$

where  $r_1$  is the radius of a PVB with ring-shaped intensity profile at the focal plane and  $\varphi_1 = \pi/10$ .  $N$  is an integer ( $N > 3$ ), which is corresponding to the  $C_N$ -fold rotational symmetry of the generated THz PVBs. For the first step of coordinate transformations (that is encoded into the Fourier transform lens with the phase  $\varphi_{\text{Step1}} = -\frac{2\pi}{\lambda} (\sqrt{(r_{11} - r_\phi)^2 + f^2} - f) + l_L \phi$ ) and  $r_{11} = \sqrt{x_1^2 + y_1^2}$ , a PVB with ring-shaped intensity profile can be transformed into a PVB with  $C_N$ -fold rotationally symmetric intensity profile. However, such a PVB (with  $C_N$ -fold rotationally symmetric intensity profiles) will generate  $N$ -fold focal spots located at each apical angle of a polygon (with  $C_N$ -fold rotational symmetry). In order to generate a PVB with  $C_N$ -fold rotationally symmetric and relatively homogeneous intensity profile, the second step (see the

phase requirement (blue-dot curve) in Figure 1b) of coordinate transformations is introduced into the axicon lens

$$x_2 = (r_\phi - r_2) \cos(\varphi_2 + \phi) \quad (5)$$

$$y_2 = (r_\phi - r_2) \sin(\varphi_2 + \phi) \quad (6)$$

where  $r_2$  is the radius of a PVB with ring-shaped intensity profile at the plane that detect the PVB, and  $\varphi_2 = \pi/5$ . By encoding the first and second steps (with the phase  $\varphi_{\text{Step2}} = -\frac{2\pi}{d} (r_{22} - r_\phi) + l_L \phi$  and  $r_{22} = \sqrt{x_2^2 + y_2^2}$ ) of coordinate transformations into a metasurface (see the phase requirement of the green curve in Figure 1b), it can generate a PVB with  $C_N$ -fold rotationally symmetric and relatively homogeneous intensity profile (The detailed design/principle for generating a PVB with  $C_N$ -fold rotationally symmetric and relatively homogeneous intensity profile is shown in Section S1, Supporting Information). Figure 1c shows the comparison of intensity distributions (of PVBs with topological charge of 1) of metasurfaces with only the first and two-step coordinate transformations, respectively. The corresponding phase requirements ( $\varphi_{\text{Step1}}$ ,  $\varphi_{\text{Step2}}$ , and  $\varphi_{\text{Step1}} + \varphi_{\text{Step2}}$ ) and intensity distributions for the PVB with topological charge of 2 and  $C_N$ -fold rotationally symmetric intensity profile are shown in Section S2, Supporting Information.

To realize the above-mentioned functionalities, geometric metasurfaces consisting of identical meta-atoms (Figure 1d) but different orientations (rotation angle of each meta-atom is  $\alpha = \Phi/2$ , where  $\Phi$  is the phase requirement for generating THz PVBs with  $C_N$ -fold rotationally symmetric or arbitrary profiles) are designed to demonstrate these unique properties. Figure 1e (top figure) shows the transmission spectra of an anisotropic silicon-based meta-atom under the illumination of the TM ( $x$ -polarized) and TE ( $y$ -polarized) THz waves. The transmittances for TM and TE waves at 0.6 THz are 89% and 91%, while the phase difference between them is about  $\pi$  (the green curve in Figure 1e). As a result, the designed meta-atom at 0.6 THz can be considered as a quasi-half waveplate. As shown by Figure 1e (the orange curve of the bottom figure) for the RCP incident THz waves, the conversion efficiency (that can be defined as the ratio between the power of the transmitted LCP THz waves and the incident power) is 90% at 0.6 THz. The optimized structural parameters are  $P = 120$   $\mu\text{m}$ ,  $W = 35$   $\mu\text{m}$ ,  $L = 99$   $\mu\text{m}$ ,  $H_1 = 500$   $\mu\text{m}$ ,  $H_2 = 500$   $\mu\text{m}$  (Figure 1d). The fabricated samples are shown in Section S3, Supporting Information.

### 3. Results

To elucidate the mechanism of a PVB with transmutable intensity profile, the helicity-dependent PVBs with  $C_5$ -fold rotationally symmetric intensity profiles are demonstrated, as shown in **Figure 2**. Two dielectric metasurfaces consisting of anisotropic silicon-based meta-atoms with identical shape but different orientations are designed and experimentally demonstrated. Each metasurface consists of  $150 \times 150$  dielectric meta-atoms, and the designed working frequency is 0.6 THz. The focal length of the Fourier transform lens is theoretically designed as  $f = 15$  mm. Figure 2a1 shows the simulated intensity distribution of the designed metasurface (with predesigned topological charge of

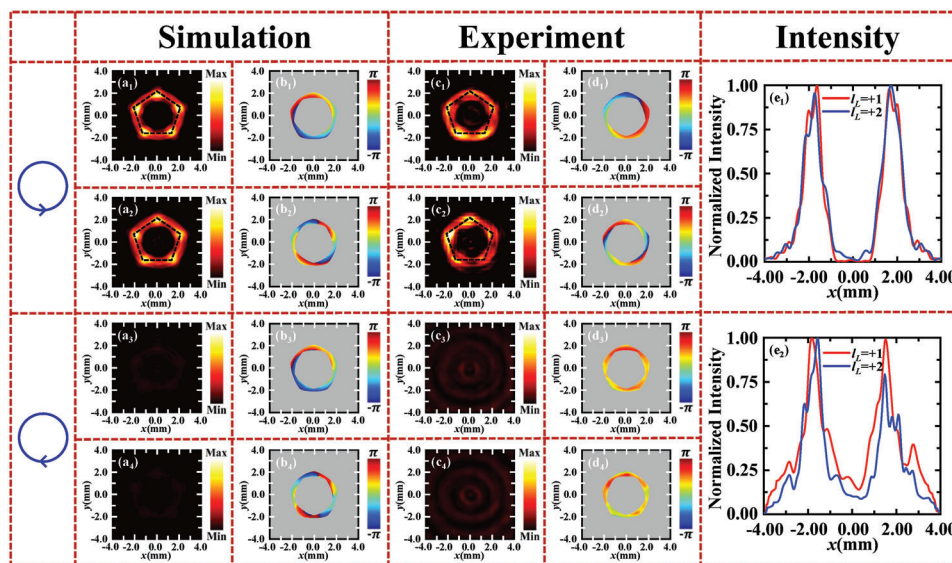


**Figure 2.** The numerical and measured intensity and phase distributions of metasurfaces for generating helicity-dependent PVBs. (a1,a2) The calculated intensity distributions (under the illumination of LCP THz waves) of metasurfaces with predesigned topological charges of  $l_L = +1$  and  $l_L = +2$ ; b1,b2) The corresponding phase distributions for (a1) and (a2). a3,b3,a4,b4) The calculated intensity ((a3) and (a4)) and phase ((b3) and (b4)) distributions for the incidence of RCP THz waves. e1) The calculated intensity distributions at line  $y = 0.8$  mm (for (a1) and (a2)). c1,c2) The measured intensity distributions (under the illumination of LCP THz waves) of metasurfaces with predesigned topological charges of  $l_L = +1$  and  $l_L = +2$ ; d1,d2) The corresponding phase distributions for (c1) and (c2). c3,d3,c4,d4) The measured intensity ((c3) and (c4)) and phase ((d3) and (d4)) distributions for the incidence of RCP THz waves. e2) The measured intensity distributions at line  $y = 0.8$  mm (for (c1) and (c2)).

$l_L = 1$ ) under the illumination of LCP THz waves. For the modulation of spiral phase plate, Fourier transform lens, axicon lens and the extra nonlinear-phase ( $\varphi_{\text{Step1}} + \varphi_{\text{Step2}}$ ), a vortex beam with pentagonal intensity profile is observed at 15 mm after the metasurface. The phase distribution of such a vortex beam is shown in Figure 2b1. The corresponding phase distribution across a turn is  $2\pi$ , which means that the vortex beam with pentagonal intensity profile possesses the topological charge of  $+1$ . When a metasurface (with predesigned topological charge of  $l_L = +2$ ) is under the shining of LCP THz waves, a vortex beam with pentagonal intensity profile is observed at 15 mm, as shown in Figure 2a2. The phase distribution of such vortex beam is numerically shown in Figure 2b2, and there are two phase jumps from  $-\pi$  to  $\pi$  (in the closed pentagonal-loop), demonstrating the topological charge of  $+2$ . The normalized intensity distributions at  $y = 0.8$  mm for the two calculated PVBs are shown in Figure 2e1. For a metasurface with predesigned topological charge of  $l_L = +1$ , the distance between the left and right boundaries (of the PVB) is 4.4 mm, while it is 4.5 mm for the vortex beam generated from the metasurface with predesigned topological charge of  $l_L = +2$ . This means that both of the vortex beams (with topological charges of  $l_L = +1$  and  $l_L = +2$ ) located at  $z = 15$  mm are the PVBs. In contrast, under the illumination of RCP THz waves, none of a vortex beam can be observed, as demonstrated in Figure 2a3–b4. In experiment, a near-field scanning terahertz microscopy (NSTM) is applied to detect intensity distributions of the fabricated sample (see the measurement method illustrated in Experimental Section.). As shown by Figure 2c1,c2 for the LCP incident THz waves, the metasurfaces (with predesigned topological charges of  $l_L = +1$  (Figure 2c1) and  $l_L = +2$  (Figure 2c2)) can simultaneously generate a vortex beam located at  $z = 15$  mm.

The corresponding phase distributions across a turn are  $2\pi$  and  $4\pi$  (in Figure 2d1,d2), demonstrating the topological charges of  $l_L = +1$  and  $l_L = +2$ , respectively. For the incidence of RCP THz waves, none of a vortex beam is generated, as experimentally demonstrated in Figure 2c3–d4. The measured distances between the left and right boundaries (at line  $y = 0.8$  mm) are 4.16 and 4.1 mm, which demonstrates that these two measured vortex beams are PVBs. The numerical simulations agree well with the measured results except for a slight discrepancy in intensity distributions, which can be attributed to the sample imperfection. The calculated (spin-dependent) PVBs with the topological charges of  $l_L = +3$ ,  $+4$  are also given in Section S4, Supporting Information.

In addition to generate spin-dependent PVBs with transmutable intensity profiles, our proposed approach can be applied to design metasurfaces to generate spin-independent PVBs with transmutable intensity profiles by designing spin-decoupled metasurfaces. The theoretical model for generating helicity-independent PVBs with transformable intensity profiles is given in Section S5, Supporting Information. The calculated results and experimental demonstration of spin-independent PVBs are shown in Figure 3. For the incidence of LCP THz waves, a vortex beam with pentagonal intensity profiles is observed at  $z = 15$  mm (after the designed metasurface), as shown in Figure 3a1. The calculated topological charge (of  $l = +1$ ) can be extracted from the corresponding phase distribution, as shown in Figure S8, Supporting Information (in Section S6, Supporting Information). For the incident THz waves with polarization switching from LCP to LCEP (left-handed elliptically polarized), LP (linearly polarized), RECP (right-handed elliptically polarized) and RCP, the phase distributions at  $z = 15$  mm still show a vortex beam with

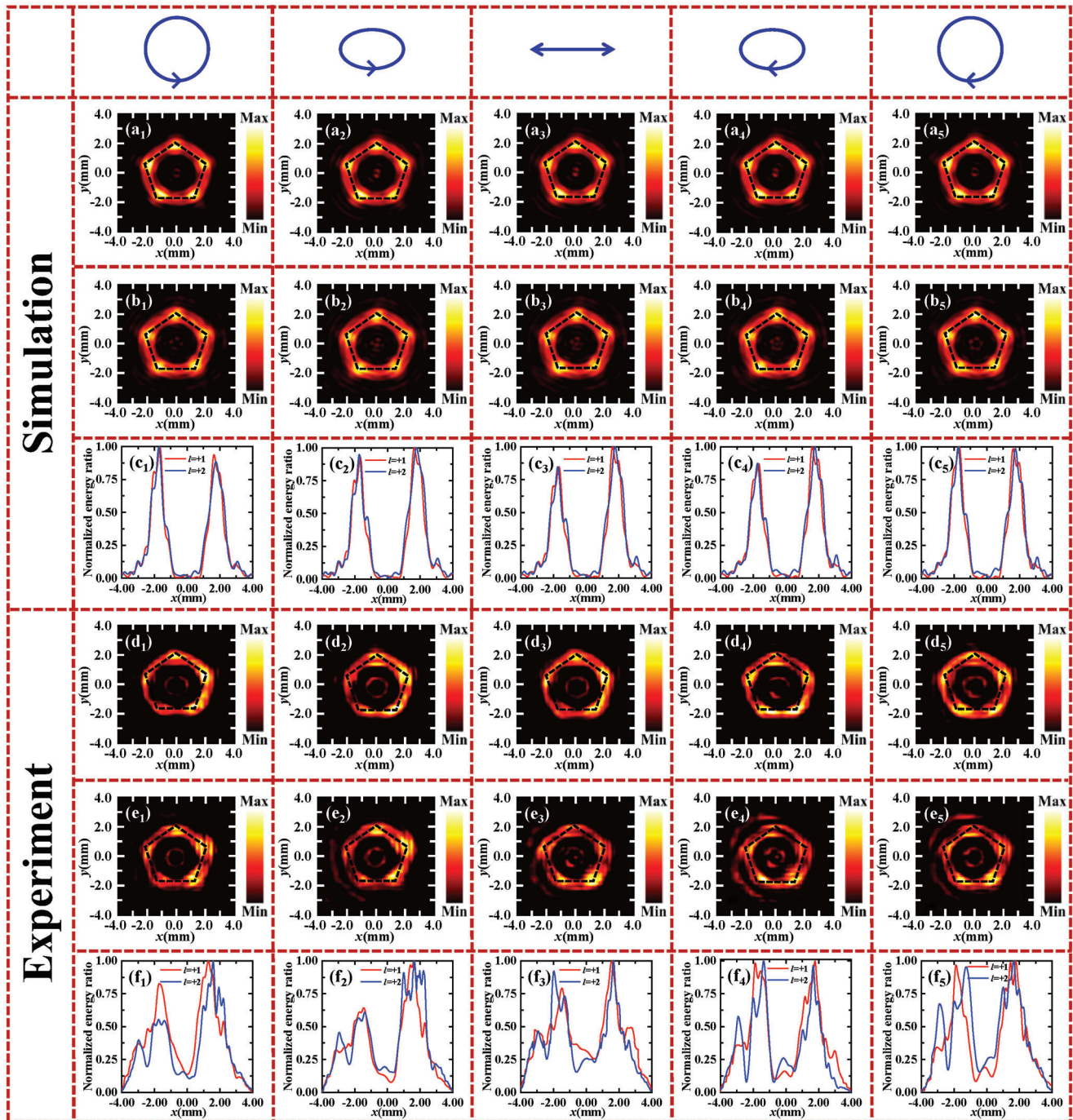


**Figure 3.** The numerical and measured intensity and phase distributions of metasurfaces for generating helicity-independent PVBs. a1–a5) The calculated intensity distributions (under the illumination of THz waves with polarization switching from LCP to LECP, LP, RECP, and RCP) of the metasurface with pre-designed topological charges of  $l_L = l_R = l = +1$ . b1–b5) The calculated intensity distributions (under the illumination of THz waves with polarization switching from LCP to LECP, LP, RECP, and RCP) of the metasurface with pre-designed topological charges of  $l_L = l_R = l = +2$ . c1–c5) The calculated intensity distributions at line  $y = 0.8$  mm. d1–d5) The measured intensity distributions (under the illumination of THz waves with polarization switching from LCP to LECP, LP, RECP, and RCP) of the metasurface with pre-designed topological charges of  $l_L = l_R = l = +1$ . e1–e5) The measured intensity distributions (under the illumination of THz waves with polarization switching from LCP to LECP, LP, RECP, and RCP) of the metasurface with pre-designed topological charges of  $l_L = l_R = l = +2$ . f1–f5) The measured intensity distributions at line  $y = 0.8$  mm.

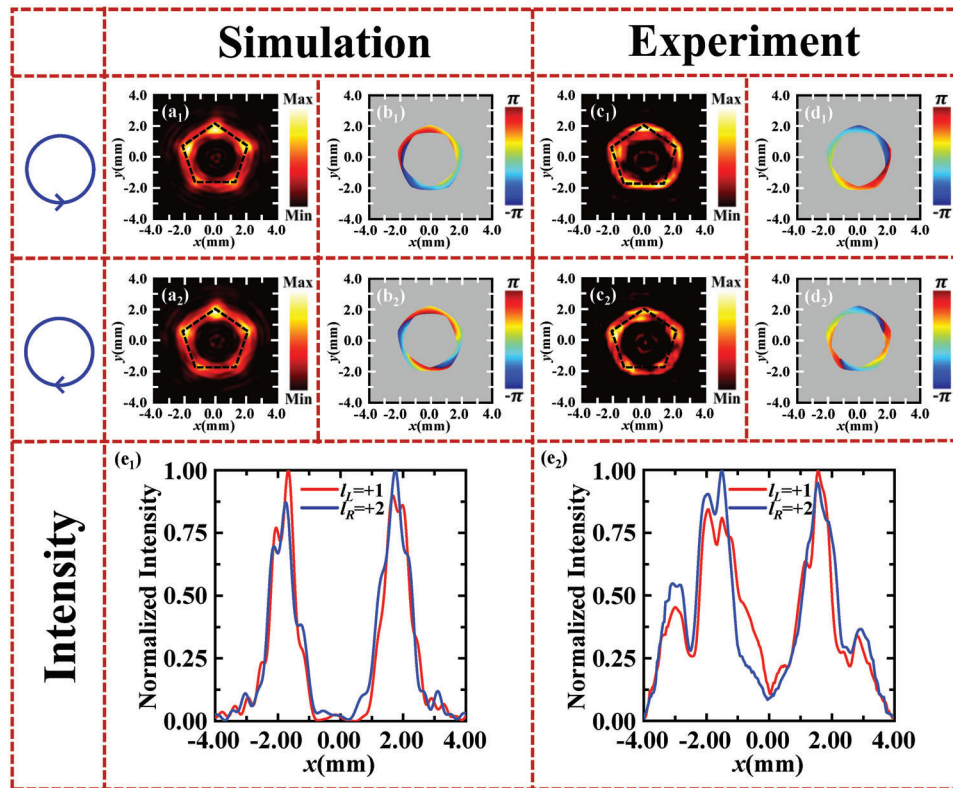


**Figure 4.** The numerical and measured intensity and phase distributions of metasurfaces for generating helicity-independent PVBs with different topological charges. a1,c1) The calculated and measured intensity distributions (under the illumination of LCP THz waves) of metasurfaces with predesigned topological charges of  $l_L = +1$ . b1,d1) The corresponding phase distributions for (a1) and (c1). e1) The calculated intensity distributions at line  $y = 0.8$  mm (for (a1) and (a2)). a2,c2) The calculated and measured intensity distributions (under the illumination of RCP THz waves) of metasurfaces with predesigned topological charges of  $l_R = +2$ . b2,d2) The corresponding phase distributions for (a2) and (c2). e2) The measured intensity distributions at line  $y = 0.8$  mm (for (a2) and (c2)).

topological charge of  $l = +1$  (see Figure S8a1–a5, Supporting Information in Section S6, Supporting Information) and pentagonal intensity profile, as shown in Figure 3a2–a5. To prove the generated vortex beam is a PVB, another spin-decoupled metasurface, which can generate a vortex beam with topological charge of  $l = +2$  and pentagonal intensity profile, is designed with the calculated electric-field intensities in Figure 3b1–b5. It should be noted that a vortex beam with topological charge of  $l = +2$  (see Figure S8b1–b5, Supporting Information in Section S6, Supporting Information) and pentagonal intensity profile can be still observed located at  $z = 15$  mm for the incident THz waves with polarization switching from LCP to RCP. The normalized intensity distributions at line  $y = 0.8$  mm for these two types of vortex beams are shown in Figure 3c1–c5. For the vortex beams with topological charge of  $l = +1$ , the distance between the left and right boundaries (at line  $y = 0.8$  mm) is nearby 4.4 mm, while it is nearby 4.5 mm for the vortex beams with topological charge of  $l = +2$ , which demonstrates that the generated vortex beams are the PVBs. The experimental demonstration of spin-independent PVBs with topological charges of  $l = +1$ ,  $l = +2$  and pentagonal intensity profile are shown in Figures 3d1–d5 and 3e1–e5, respectively. Under the illumination of THz waves with polarization switching from LCP to RCP, there is always a vortex beam with pentagonal intensity profile that can be ob-

served located at  $z = 15$  mm. The distances between the left and right boundaries at line  $y = 0.8$  mm are 4.3 and 4.4 mm for the vortex beams with topological charges of  $l = +1$ ,  $l = +2$ , respectively. The topological charge of each measured vortex beam is given in Figures S8c1–d5, Supporting Information (in Section S6, Supporting Information). In addition, the spin-independent PVBs with topological charges of  $l = +3$ ,  $l = +4$ , and pentagonal intensity profile are also calculated shown in Figure S9, Supporting Information (in Section S7, Supporting Information).

The proposed approach cannot only design metasurfaces that can generate PVBs with orthogonal helicity and identical topological charges, but also enables the capability in designing metasurfaces to generate PVBs with orthogonal helicity and different topological charges. As depicted in Equation (S7), Supporting Information, two PVBs with orthogonal helicity and different topological charges can be obtained for  $l_L \neq l_R \neq 0$ . As shown by Figure 4a1 for the incident LCP THz waves, a vortex beam (located at  $z = 15$  mm) with pentagonal intensity profile is observed. The phase distribution of this vortex beam is shown in Figure 4b1, and the phase distribution across a turn is  $2\pi$ , which means that the topological charge of the vortex beam (shown in Figure 4a1) is  $l_L = +1$ . For the incidence of RCP THz waves, there is also a vortex beam (located at  $z = 15$  mm) with pentagonal intensity

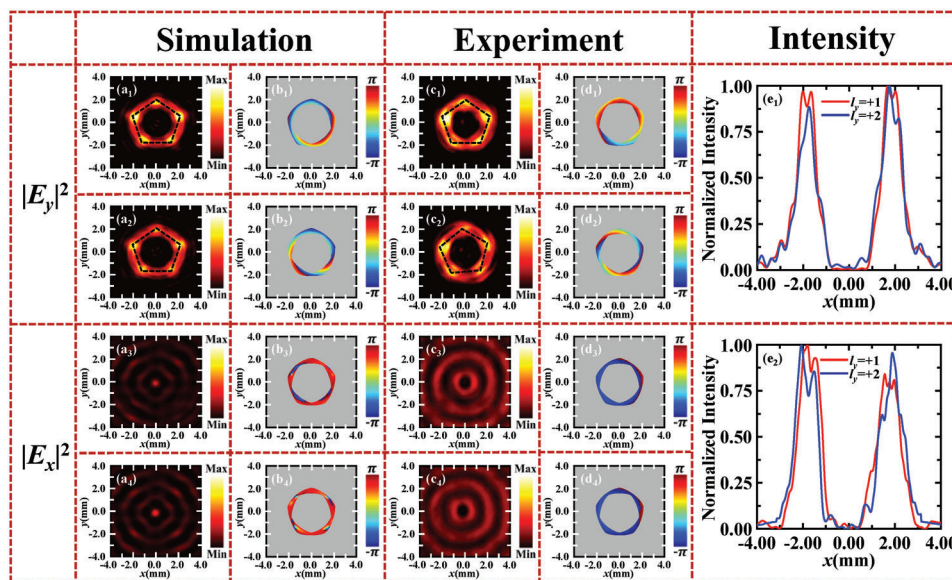


**Figure 5.** The numerical and measured intensity and phase distributions of metasurfaces for generating polarization-rotated PVBs. a1,a2) The calculated  $y$ -polarized intensity distributions for metasurfaces with predesigned topological charges of +1 and +2, and under the illumination of  $x$ -polarized THz waves. b1,b2) The corresponding phase distributions for (a1) and (a2). a3,a4) The calculated  $x$ -polarized intensity distributions for metasurfaces with predesigned topological charges of +1 and +2, and under the illumination of  $x$ -polarized THz waves. b3,b4) The corresponding phase distributions for (a3) and (a4). c1,c2) The measured  $y$ -polarized intensity distributions for metasurfaces with predesigned topological charges of +1 and +2, and under the illumination of  $x$ -polarized THz waves. d1,d2) The corresponding phase distributions for (c1) and (c2). c3,c4) The measured  $x$ -polarized intensity distributions for metasurfaces with predesigned topological charges of +1 and +2, and under the illumination of  $x$ -polarized THz waves. d3,d4) The corresponding phase distributions for (c3) and (c4). e1) The calculated intensity distributions at line  $\gamma = 0.8$  mm (for (a1) and (a2)). e2) The measured intensity distributions at line  $\gamma = 0.8$  mm (for (c1) and (c2)).

profile appeared after the metasurface, as shown in Figure 4a2. The corresponding phase distribution (shown in Figure 4b2) (of such a vortex beam) across a turn is  $4\pi$ , which demonstrates that the topological charge of this vortex beam is  $l_R = +2$ . The distances between the left and right boundaries at line  $\gamma = 0.8$  mm are 4.4 mm and 4.5 mm (see Figure 4e1) for the calculated vortex beams with topological charges of  $l_L = +1$ ,  $l_R = +2$ , respectively. Therefore, the two vortex beams (in Figure 4a1,a2) are the PVBs. The experimental demonstration of spin-independent PVBs with different topological charges is shown in Figure 4c1,c2, respectively. Under the illumination of LCP/RCP THz waves, a vortex beam with pentagonal intensity profile can be observed, and the corresponding topological charge is  $l_L = +1/l_R = +2$  (see phase distributions in Figure 4d1,d2), respectively. In addition, the measured distances between the left and right boundaries at line  $\gamma = 0.8$  mm are 4.4 and 4.6 mm (see Figure 4e2) for the vortex beams with topological charges of  $l_L = +1$ ,  $l_R = +2$ , which means that the two vortex beams are PVBs. The metasurfaces to generate PVBs with orthogonal helicity and topological charges of  $l_L = +3$  and  $l_R = +4$  are also designed and calculated in Figure S10, Supporting Information (see Section S8, Supporting Information).

The polarization-independent PVBs (in Figure 3) demonstrated above can be indeed realized by focusing two orthogonal helical-components together with the same topological charge. Therefore, for the incident of LP THz waves, a LP PVB with the same polarization (compared with the polarization of the incident LP THz waves) can be obtained. In addition to realize LP-based PVB with the cross-polarization (compared with the

incident THz waves), our proposed approach can generate a LP-based PVB with polarization-rotated functionality. The theoretical model for generating polarization-rotated PVBs with transformable intensity profiles is given in Section S5, Supporting Information. As shown by Figure 5a1 for the  $x$ -polarized incident THz waves, a  $y$ -polarized vortex beam located at  $z = 15$  mm is obtained (for  $\theta = 90^\circ$ ). The corresponding phase distribution (shown in Figure 5b1) of such vortex beam demonstrates that the topological charge (of this vortex beam) is +1. In the same way, another  $y$ -polarized vortex beam located at  $z = 15$  mm is observed under the illumination of  $x$ -polarized THz waves, as shown in Figure 5a2. Figure 5b2 shows the corresponding phase distribution, and the topological charge of such a vortex beam is +2. The distances between the left and right boundaries at line  $\gamma = 0.8$  mm (for the calculated vortices with topological charges of +1 and +2) are 4.5 and 4.5 mm, which demonstrates that these two vortex beams are PVBs. In contrast, the  $x$ -polarized electric-intensity and phase distributions shown in Figure 5a3–b4 reveal that none of an  $x$ -polarized vortex beam is generated. Therefore, for the incidence of  $x$ -polarized THz waves, the generated PVBs are polarization-rotated ( $y$ -polarized) PVBs. Figure 5c1,c2 show the measured  $y$ -polarized electric-field intensity distributions for metasurfaces (with predesigned topological charge of +1 (Figure 5c1) and +2 (Figure 5c2)) under the illumination of  $x$ -polarized THz waves. A vortex beam is still observed (at  $z = 15$  mm) after the metasurface, and the corresponding topological charge is +1 (see Figure 5d1) or +2 (see Figure 5d2). The distances between the left and right boundaries at line  $\gamma = 0.8$  mm (for the measured vortices with topological charges of +1 and

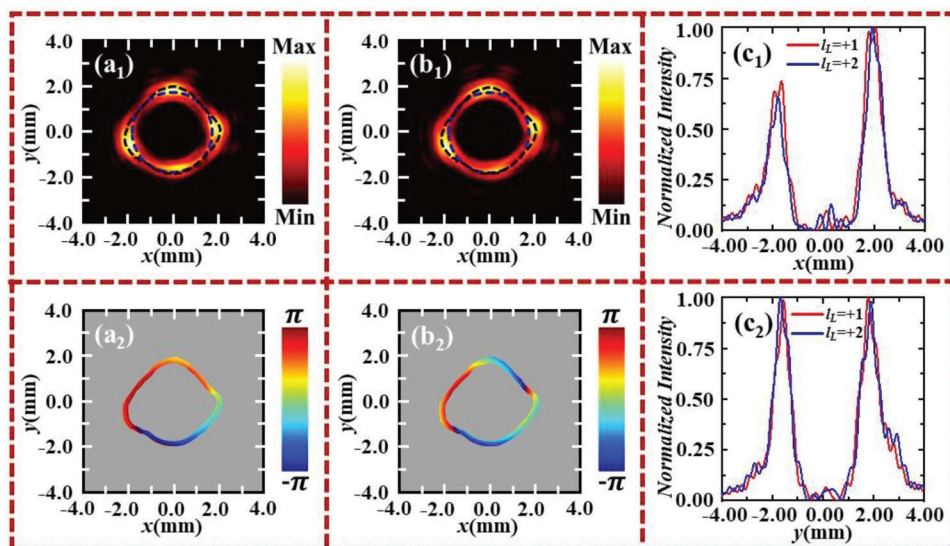


**Figure 6.** The calculated intensity and phase distributions of metasurfaces for generating PVBs with arbitrary intensity profiles. a1,b1) The calculated intensity distributions for metasurfaces with predesigned topological charges of +1 and +2, and under the illumination of LCP THz waves. a2,b2) The corresponding phase distributions for (a1) and (a2). c1) The calculated intensity distributions at line  $y = 0$  (for (a1) and (b1)). c2) The calculated intensity distributions at line  $x = 0$  (for (a1) and (b1)). The blue dot lines in (a1) and (b1) are the central of PVBs without deformation, while the black dot lines in (a1) and (b1) are the central of PVBs with two steps of coordinate transformations (in Equations (S3) and (S4), Supporting Information).

+2) are 4.5 mm and 4.7 mm, which means that these two vortex beams are PVBs. For the incidence of  $x$ -polarized THz waves, there is no ( $x$ -polarized) vortex beam, as shown in Figure 5c3–d4. The polarization-rotated PVBs with topological charges of +3 and +4 are also calculated in Figure S11, Supporting Information (see Section S9, Supporting Information).

#### 4. Discussion

In addition to generate PVBs with  $C_N$ -fold rotationally symmetric intensity profiles, the robust approach enables the capability to design geometric metasurfaces that can generate PVBs with arbitrary intensity profiles. The theoretical model for generating PVBs with arbitrary intensity profiles is given in Section S5, Supporting Information. In addition, the detailed design/principle for generating a PVB with arbitrary and relatively homogeneous intensity profile is shown in Section S1, Supporting Information.

According to Equation (S3), Supporting Information, three humps at  $\phi = 0, \frac{\pi}{2}, \frac{13}{12}\pi$  can be observed in the generated PVBs. The second step (Equation (S10), Supporting Information) is introduced to avoid inhomogeneous intensity distributions (In other words, the second step is added to generate a PVB with relatively homogeneous intensity profile). The numerical demonstration of PVBs with arbitrary intensity profiles is shown in **Figure 6**. As shown by Figure 6a1 for the LCP incidence of THz waves, a vortex beam with three humps is observed at  $z = 15$  mm. The phase distribution of this vortex beam is shown in Figure 6a2, and the topological charge (of this vortex beam) is +1, since the corresponding phase jumps from  $-\pi$  to  $\pi$ . For the designed metasurface with predesigned topological charge of +2, a vortex beam after the metasurface (at  $z = 15$  mm) is also observed under the

illumination of LCP THz waves (see Figure 6b1). The calculated phase distribution in Figure 6b2 also demonstrates that the topological charge of this vortex beam is +2. The distances between the left and right boundaries at line  $y = 0$  (for the calculated vortices with topological charges of +1 and +2) are 4.3 and 4.4 mm, while the distances are 4.2 and 4.3 mm at line  $x = 0$ , which demonstrates that the generated vortex beams are PVBs. In addition, the polarization-dependent (or polarization-independent) PVBs with arbitrary intensity profiles and topological charges of +3 and +4 (or +1, +2, +3, +4) are given in Section S10, Supporting Information.

#### 5. Conclusion

In summary, we have proposed and demonstrated a robust approach to design geometric metasurfaces for generating PVBs with  $C_N$ -fold rotationally symmetric and arbitrary intensity profiles. The realization of PVBs with transmutable intensity profiles was dependent on two-step coordinate transformations, where the first step was designed to manipulate the corresponding intensity profiles while the second step was optimized to generate relatively homogeneous intensity profiles. By encoding the functionalities of a spiral phase plate, Fourier transform lens, axicon lens and two nonlinear phase requirements (generated from two-step coordinate transformations), the polarization-dependent/independent and polarization-rotated PVBs with  $C_N$ -fold rotationally symmetric intensity profiles were demonstrated. Furthermore, PVBs with arbitrary intensity profiles were also demonstrated. The robust approach for simultaneously generating and manipulating PVBs and the corresponding intensity profiles, would open up a new avenue to design multifunctional flat-devices with applications in particle manipulation and information encoding and transmission.



## 6. Experimental Section

A NSTM (see the schematic in Section S11, Supporting Information) was built up to measure electric-field intensity distributions of the designed metasurfaces. A femtosecond laser beam with central wavelength of 780 nm was split into two parts. One part of the laser beam was focused onto a photoconductive antenna that can excite THz radiation. The other part of the laser beam was coupled into a single-mode fiber and then shined onto a THz tip that was applied to detect electric-field intensity distributions of metasurfaces. The THz tip was mounted on a 3D translation stage. The fabricated samples were fixed after the photoconductive antenna, while the THz tip was scanned after the samples to collect the electric-field intensity distributions.

## Supporting Information

Supporting Information is available from the Wiley Online Library or from the author.

## Acknowledgements

This work was supported by the National Key Research and Development Program of China (2017YFA0701005), National Natural Science Foundation of China (62271320, 61871268), “Shuguang” Program of Shanghai Education Commission (19SG44), the project from Shanghai Municipal Science and Technology Commission (22JC1400200), and the 111 Project (D18014). The data computing platform are provided by the “SciPlus with Universities” project. Thanks to the project sponsor “Shanghai Science and Technology Innovation Resources Center (SSTIR)” and the organizer “Shanghai Science and Technology Development Co., LTD. (SSTD).”

## Conflict of Interest

The authors declare no conflict of interest.

## Author Contributions

X.Z. conceived the initial idea. B.S. conducted the numerical simulations. B.S. and B.L. performed the measurements. B.S., X.Z., and Y.Z. analyzed the data. All authors read and approved the final manuscript.

## Data Availability Statement

The data that support the findings of this study are available from the corresponding author upon reasonable request.

## Keywords

geometric phase, metasurfaces, orbital angular momentum, perfect vortices, transmutable intensity profiles

Received: May 4, 2023

Revised: June 16, 2023

Published online:

[1] L. Allen, M. W. Beijersbergen, R. J. Spreeuw, J. P. Woerdman, *Phys. Rev. A* **1992**, *45*, 8185.

- [2] Q. Zhan, *Adv. Opt. Photonics* **2009**, *1*, 1.
- [3] R. Fickler, R. Lapkiewicz, W. N. Plick, M. Krenn, C. Schaeff, S. Ramelow, A. Zeilinger, *Science* **2012**, *338*, 640.
- [4] J. Wang, J. Yang, I. M. Fazal, N. Ahmed, Y. Yan, H. Huang, Y. Ren, Y. Yue, S. Dolinar, M. Tur, A. E. Willner, *Nat. Photonics* **2012**, *6*, 488.
- [5] J. E. Curtis, D. G. Grier, *Phys. Rev. Lett.* **2003**, *90*, 133901.
- [6] P. Li, Y. Zhang, S. Liu, C. Ma, L. Han, H. Cheng, J. Zhao, *Opt. Lett.* **2016**, *41*, 2205.
- [7] A. S. Ostrovsky, R. P. Carolina, A. Víctor, *Opt. Lett.* **2013**, *38*, 534.
- [8] V. Pravin, R. Leslie, *Opt. Lett.* **2015**, *40*, 597.
- [9] M. Z. Chen, M. Mazilu, Y. Arita, W. M. Wright, K. Dholakia, *Opt. Lett.* **2013**, *38*, 4919.
- [10] M. V. Jabir, N. A. Chaitanya, A. Aadhi, G. K. Samanta, *Sci. Rep.* **2016**, *6*, 21877.
- [11] D. Li, S. Feng, S. Nie, C. Chang, J. Ma, C. Yuan, *J. Appl. Phys.* **2019**, *125*, 073105.
- [12] L. Huang, X. Chen, H. Mühlenbernd, G. Li, B. Bai, Q. Tan, G. Jin, T. Zentgraf, S. Zhang, *Nano Lett.* **2012**, *12*, 5750.
- [13] X. Zang, B. Yao, L. Chen, J. Xie, X. Guo, A. V. Balakin, A. P. Shkurinov, S. Zhuang, *Light: Adv. Manuf.* **2021**, *2*, 10.
- [14] N. Yu, P. Genevet, M. A. Kats, F. Aieta, J. P. Tetienne, F. Capasso, Z. Gaburro, *Science* **2011**, *334*, 333.
- [15] X. Ni, N. K. Emani, A. V. Kildishev, A. Boltasseva, V. M. Shalaev, *Science* **2012**, *335*, 427.
- [16] Z. Liu, Z. Li, Z. Liu, J. Li, H. Cheng, P. Yu, W. Liu, C. Tang, C. Gu, J. Li, S. Chen, J. Tian, *Adv. Funct. Mater.* **2015**, *25*, 5428.
- [17] N. K. Grady, J. E. Heyes, D. R. Chowdhury, Y. Zeng, M. T. Reiten, A. K. Azad, A. J. Taylor, D. A. R. Dalvit, H.-T. Chen, *Science* **2013**, *340*, 1304.
- [18] R. Fan, Y. Zhou, X. Ren, R. Peng, S. Jiang, D. Xu, X. Xiong, X. Huang, M. Wang, *Adv. Mater.* **2015**, *27*, 1201.
- [19] X. Zang, H. Gong, Z. Li, J. Xie, Q. Cheng, L. Chen, A. P. Shkurinov, Y. Zhu, S. Zhuang, *Appl. Phys. Lett.* **2018**, *112*, 171111.
- [20] X. Ling, X. Zhou, X. Yi, W. Shu, Y. Liu, S. Chen, H. Luo, S. Wen, D. Fan, *Light: Sci. Appl.* **2015**, *4*, e290.
- [21] W. Luo, S. Xiao, Q. He, S. Sun, L. Zhou, *Adv. Opt. Mater.* **2015**, *3*, 1102.
- [22] X. Zang, B. Yao, Z. Li, Y. Zhu, J. Y. Xie, L. Chen, S. Han, Y. Zhu, S. Zhuang, *Nanophotonics* **2020**, *9*, 1501.
- [23] X. Chen, L. Huang, H. Mühlenbernd, G. Li, B. Bai, Q. Tan, G. Jin, C. Qiu, S. Zhang, T. Zentgraf, *Nat. Commun.* **2012**, *3*, 1198.
- [24] A. Arbabi, Y. Horie, M. Bagheri, A. Faraon, *Nat. Nanotechnol.* **2015**, *10*, 937.
- [25] M. Khorasaninejad, W. Chen, R. C. Devlin, J. Oh, A. Zhu, F. Capasso, *Science* **2016**, *352*, 1190.
- [26] R. J. Lin, V. C. Su, S. Wang, M. K. Chen, T. L. Chung, Y. H. Chen, H. Y. Kuo, J. W. Chen, J. Chen, Y. T. Huang, J. H. Wang, C. H. Chu, P. C. Wu, T. Li, Z. Wang, S. Zhu, D. P. Tsai, *Nat. Nanotechnol.* **2018**, *14*, 227.
- [27] W. Chen, A. Zhu, V. Sanjeev, M. Khorasaninejad, Z. Shi, E. Lee, F. Capasso, *Nat. Nanotechnol.* **2019**, *13*, 220.
- [28] X. Zang, H. Ding, Y. Intaravanne, L. Chen, Y. Peng, Q. Ke, A. V. Balakin, A. P. Shkurinov, X. Chen, Y. Zhu, S. Zhuang, *Laser Photonics Rev.* **2019**, *13*, 1900182.
- [29] X. Zang, W. Xu, M. Gu, B. Yao, L. Chen, Y. Peng, J. Xie, A. V. Balakin, A. P. Shkurinov, Y. Zhu, S. Zhuang, *Adv. Opt. Mater.* **2020**, *8*, 1901342.
- [30] R. Wang, Y. Intaravanna, S. Li, J. Han, S. Chen, J. Liu, S. Zhang, L. Li, X. Chen, *Nano Lett.* **2021**, *21*, 2081.
- [31] X. Ni, A. V. Kildishev, V. M. Shalaev, M. Vladimir, *Nat. Commun.* **2013**, *4*, 2807.
- [32] G. Zheng, H. Mühlenbernd, M. Kenney, G. Li, T. Zentgraf, S. Zhang, *Nat. Nanotechnol.* **2015**, *10*, 308.

- [33] D. Wen, F. Yue, G. Li, G. Zheng, K. Chan, S. Chen, M. Chen, K. F. Li, P. W. H. Wong, K. W. Cheah, E. Y. B. Pun, S. Zhang, X. Chen, *Nat. Commun.* **2015**, *6*, 8241.
- [34] L. Jin, Z. Dong, S. Mei, Y. Yu, Z. Wei, Z. Pan, S. D. Rezaei, X. Li, A. I. Kuznetsov, Y. S. Kivshar, J. K. W. Yang, C. W. Qiu, *Nano Lett.* **2018**, *18*, 8016.
- [35] I. Kim, J. Jang, G. Kim, J. Lee, T. Badloe, J. Mun, J. Rho, *Nat. Commun.* **2021**, *12*, 3614.
- [36] H. Wang, Z. Qin, L. Huang, Y. Li, R. Zhao, H. Zhou, H. He, J. Zhang, S. Qu, *PhotonIX* **2022**, *3*, 10.
- [37] H. Cheng, Z. Liu, S. Chen, J. Tian, *Adv. Mater.* **2015**, *27*, 5410.
- [38] R. C. Devlin, A. Ambrosio, N. A. Rubin, J. P. B. Mueller, F. Capasso, *Science* **2017**, *358*, 896.
- [39] X. Zang, Y. Zhu, C. Mao, W. Xu, H. Ding, J. Xie, L. Chen, S. Han, Y. Zhu, S. Zhuang, *Adv. Opt. Mater.* **2018**, *7*, 1801328.
- [40] K. Zhang, Y. Yuan, X. Ding, H. Li, B. Ratni, Q. Wu, J. Liu, S. N. Burokur, J. Tan, *Laser Photonics Rev.* **2020**, *15*, 2000351.
- [41] E. Maguid, I. Yulevich, D. Veksler, V. Kleiner, M. L. Brongersma, E. Hasman, *Science* **2016**, *352*, 1202.
- [42] S. Zhang, P. Huo, W. Zhu, C. Zhang, P. Chen, M. Liu, L. Chen, H. J. Lezec, A. Agrawal, Y. Lu, T. Xu, *Laser Photonics Rev.* **2020**, *15*, 2000062.
- [43] F. Yue, D. Wen, C. Zhang, B. D. Gerardot, W. Wang, S. Zhang, X. Chen, *Adv. Mater.* **2017**, *29*, 1603838.
- [44] Y. Zhang, J. Gao, X. Yang, *Sci. Rep.* **2019**, *9*, 9969.
- [45] P. N. Ni, P. P. Chen, C. Xu, Y. Y. Xie, P. Genevet, *Nat. Commun.* **2021**, *13*, 7795.
- [46] Y. Bao, J. Ni, C. W. Qiu, *Adv. Mater.* **2020**, *32*, 1905659.
- [47] J. Han, Y. Intaravanne, A. Ma, R. Wang, S. Li, Z. Li, S. Chen, J. Li, X. Chen, *Laser Photonics Rev.* **2020**, *14*, 2000146.
- [48] M. Liu, P. Huo, W. Zhu, C. Zhang, S. Zhang, M. Song, Q. Zhou, L. Chen, H. J. Lezec, A. Agrawal, Y. Lu, T. Xu, *Nat. Commun.* **2021**, *12*, 2230.
- [49] J. Xie, H. Guo, S. Zhuang, J. Hu, *Opt. Express* **2021**, *29*, 3081.